THE JOURNAL OF PHYSICAL CHEMISTRY C

pubs.acs.org/JPCC Article

First-Principles Prediction of Na Diffusivity in Doped $NaCrO_2$ Layered Cathode Materials with van der Waals Interactions

Jialiang Wei, Leon Shaw, and Wei Chen*

Cite This: J. Phys. Chem. C 2020, 124, 12239−12248 Read Online

ACCESS | Metrics & More | Article Recommendations | Supporting Information

ABSTRACT: The O3-layered $NaCrO_2$ is a promising Na-ion cathode material with a good thermal stability and specific capacity, but it suffers from a poor rate capability. To develop high-rate Na-ion cathodes, we present a first-principles study of the stability and Na diffusion in pure and doped $NaCrO_2$ with PBE and various functionals that explicitly include van der Waals (vdW) interactions. The interlayer distances in partially desodiated $NaCrO_2$ are significantly reduced with the inclusion of vdW interactions, which directly affects the prediction of Na diffusion barriers. A linear relation between the interlayer distance and the diffusion barrier is established with different functionals. We notice that the increased diffusion barriers are mostly due to the reduced interlayer distances predicted by the vdW-inclusive functionals rather than the inclusion of vdW interactions in the transition state calculations. Other factors such as the charge density change introduced by different dopants also have effects on the Na diffusion barriers. We find low-concentration metal doping (Al, Zn, Mn, and Co) in $NaCrO_2$ has minor effects on its thermodynamic stability but the Na diffusivity can be significantly promoted. The Co-doped $NaCrO_2$ outperforms other doped $NaCrO_2$ with lower Na diffusion barriers and can be considered as a potential candidate for high-rate Na-ion cathode materials. This study highlights the importance of vdW interactions in layered transition metal oxides and offers strategies to improve first-principles predictions for these structures.

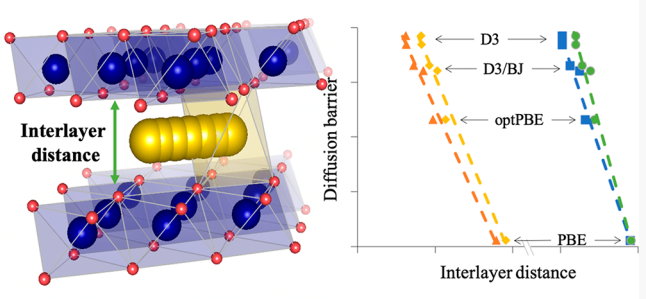

1. INTRODUCTION

Na-ion batteries (SIBs) have attracted great attention as an abundant and low-cost alternative to Li-ion batteries (LIBs), particularly as candidates for medium and large-scale stationary energy storage.[1,2] Layered transition metal (TM) oxides with the chemical formula of Na_xTMO_2 (TM is transition metal, such as Cr, Co, Ni, Mn, Ti, and Fe)[3−9] represent a family of potential cathode materials for SIBs. These layered structures are classified into two groups by the octahedral (O) or prismatic (P) arrangement of the NaO_6 polyhedra. The O3-layered structure (Figure 1a) is composed of octahedrally coordinated Na and TM ions and a periodic stacking of TM-Na-TM units.[10] Two-dimensional TMO_2 or NaO_2 layers are then formed by edge-sharing of the TMO_6 or NaO_6 octahedra. The O3−Na_xTMO_2 often retains higher resistance against phase transformations into other structures (e.g., spinel) than O3−Li_xTMO_2 upon cycling,[11] which is attributed to the larger Na interlayer distances in $NaTMO_2$.[12] Meanwhile, the higher stability of O3−Na_xTMO_2 can be related to the fact that Na ions tend to coordinate with six oxygen ions and form octahedra rather than tetrahedra as suggested by Pauling's first rule (the radius ratio rule).[11]

The O3-layered $NaCrO_2$ is a promising Na-ion cathode material, delivering a reversible capacity of 120 mA h g^{-1} and a good capacity retention[9] that is comparable to $LiCoO_2$ with a reversible capacity of 140 mA h g^{-1}.[13] However, the relatively low ionic conductivity in pure $NaCrO_2$ limits its rate capability and application as a cathode material.[9] Doping is an effective strategy to improve the electrochemical performance of TM oxide cathodes, such as voltage, structural stability, and electronic conductivity.[14−16] For instance, Al dopant increases the structural stability and intercalation potential in layered $LiCoO_2$[17] and lithium nickel oxides[18] by suppressing layer-to-spinel phase transformation. Zn dopant improves the structural reversibility in P2-layered $Na_{0.66}Ni_{0.33}Mn_{0.67}O_2$ due to the stabilization of Ni−O octahedra by Zn.[19] Both electrochemically inactive and active cation dopants have been explored to improve the rate performance of TM oxide cathodes. A previous study has shown that the Li diffusion coefficient increases by more than 1 order of magnitude in Al-doped $LiMnNiCoO_2$ compared to the undoped one.[20] The ionic diffusivity in olivine $LiFePO_4$ benefits from Zn dopants which

Received: March 15, 2020
Revised: May 13, 2020
Published: May 15, 2020

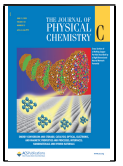

https://dx.doi.org/10.1021/acs.jpcc.0c02274
J. Phys. Chem. C 2020, 124, 12239−12248

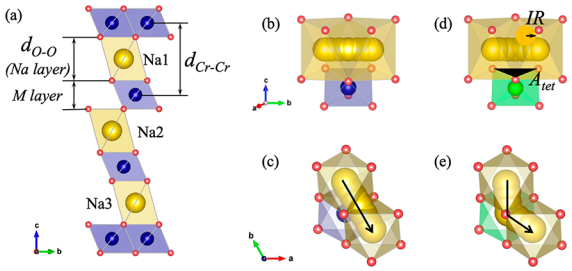

Figure 1. (a) Crystal structure of O3-$NaCrO_2$. Na, Cr, and O atoms are represented by yellow, blue, and red balls, respectively. The Na layer is the O−Na−O layer where Na migrates. The M layer is the O-M-O layer that contains Cr and the dopant atom. d_{Cr-Cr} and d_{O-O} correspond to the average M−Na−M and O−Na−O interlayer distances. Typical Na diffusion pathways in pure $NaCrO_2$ (b) side view and (c) top view and in Co-doped $NaCrO_2$ (d) side view and (e) top view. Panels b and c correspond to the oxygen dumbbell hop (ODH), while panels d and e correspond to the tetrahedral site hop (TSH). The green ball represents dopant Co atoms. A_{tet} is the area of the tetrahedron triangle face between adjacent Na octahedra. The incircle radius (IR) of the cross-sectional triangle is highlighted in orange in panel d. The black solid line in panels c and e indicates the Na diffusion pathway.

expands the cell volume and, consequently, provides more space for Li diffusion.[21] The influence of electrochemically active cations (e.g., Co, Mn, and Ni) on ionic diffusion can be quite complex. Low-valent TM cations (e.g., Ni^{2+}) can increase the ionic diffusivity because they are less electrostatically repulsive to the migrating ions, but high-valent TM cations (e.g., Mn^{4+}) are often helpful to improve the stability of the host structure.[22]

Electrode materials with lower ionic diffusion barriers and faster ionic movement possess higher rate capabilities. The divacancy ionic hopping of M (M = Li and Na) in layered $MCoO_2$ has been compared using the nudged elastic band (NEB) method.[23] Despite a larger ionic radius, Na has a lower diffusion barrier in the layered framework where the increased Na interlayer distance is considered as the key factor for diffusion barrier.[24] O3-$NaCoO_2$ has also been reported to have an appreciably lower activation barrier than P2-$NaCoO_2$ from ab initio molecular dynamics (AIMD) simulations.[25] A synergy between the large interlayer distance and the weak repulsive forces between the TM and Na ions can increase Na diffusivity.

van der Waals (vdW) interactions play an important role in binding neighboring TMO_2 layers but are often ignored in computational studies. vdW-inclusive functionals have produced more accurate predictions of layered TM oxides than conventional functionals. For example, vdW-inclusive functionals predict the voltage, stability, and structure of layered $LiCoO_2$ that shows much better agreement with experimental results.[26] However, the role of vdW interactions on the diffusion activation energy in layered TM oxides still has not been well understood. vdW-inclusive functionals have been used in calculating the diffusion activation energy of alkali and alkaline-earth ion in α-V_2O_5 and the vdW interactions have been proven not critical in determining the activation energy.[27]

The objective of this study is to understand how metal doping can improve the rate capability of $NaCrO_2$. In this study, the effects of dopant on the stability and Na diffusivity in $NaCrO_2$ are investigated with first-principles methods. Density functional theory (DFT) calculations are performed in search of doping candidates for stable high-rate capability SIB cathode materials. In particular, we will focus on elucidating the role of vdW interactions on predicting the structural parameters and Na diffusivity in doped layered $NaCrO_2$ systems with vdW-inclusive functionals.

2. METHODS

2.1. Structural Optimizations. First-principles total energy calculations were performed with DFT using the projector augmented-wave (PAW)[28] approach as implemented in the Vienna ab initio simulation package (VASP).[29,30] The exchange-correlation energy was approximated with the Perdew−Burke−Ernzerhof (PBE)[31] generalized-gradient approximation (GGA),[32] vdW corrected PBE functionals (D2,[33] D3,[34] and D3/BJ[35]), the metaGGA SCAN functional,[36] and GGA exchange-optimized vdW "opt" functionals (optB86b, optB88, and optPBE).[37] Hubbard U parameters,[38] the on-site Coulomb correction on the localized d orbitals, were applied on certain 3d transition metals to correct the total energy of TM oxides for PBE-based functionals. We adopted the U values determined by the Materials Project from fitting the experimental binary formation enthalpies of TM oxides.[39,40] The effective U value in the case of Dudarev's approach for Cr, Co, Ni, and Mn are 3.7, 3.32, 6.2, and 3.9 eV, respectively.[41] As a comparison, structural optimization of pure $NaCrO_2$ was also performed with the HSE06 hybrid functional and a mixing parameter of 0.25.[42,43] The plane wave cutoff energy was 520 eV and a Gamma-centered **k**-point mesh with a **k**-point density per reciprocal atom of at least 1000 was used. To study the effects of Cr-substitutional metal doping, the conventional cell of O3−$Na_3Cr_3O_6$ was used to build 3 × 3 × 1 supercells ($Na_{27}Cr_{27}O_{54}$) whose Cr atoms were partially substituted. All structures were optimized until the energy was converged within 10^{-4} eV per supercell and the forces on each atom were less than 0.01 eV/Å. Spin-polarization was considered in all calculations with high-spin initialization.

2.2. Thermodynamic Stability of Doped $NaCrO_2$. The stability of doped $NaCrO_2$ was studied by constructing 0 K phase diagrams with known compounds from the chemical systems.[44] For example, a Na−Cr−O-Ni quaternary phase diagram was constructed for the Ni-$NaCrO_2$ system. M-$NaCrO_2$ represents M-doped $NaCrO_2$. Relevant structures were retrieved from the Materials Project and recalculated with consistent parameters.[40] The thermodynamic stability of the doped system was assessed with the decomposition energy (E_{decomp}) above the tie-line between adjacent stable compounds. A doped $NaCrO_2$ is considered stable at room temperature when E_{decomp} is below 100 meV per 108-atom supercell.

2.3. Na Diffusion in Doped $NaCrO_2$. The diffusion barrier of Na atom in doped $NaCrO_2$ was calculated using the climbing image nudged elastic band (CI-NEB) method with PBE and vdW inclusive functionals.[45] A force convergence criterion of 0.02 eV/Å was used in CI-NEB calculations. U parameters were not applied in the CI-NEB calculations because they can introduce charge transfer barriers for ionic diffusion.[23] To identify the role of dopants on the Na diffusion barrier at a dilute Na condition, 1/9 of the Na sites in one of the Na layers was occupied with Na atoms in the CI-NEB calculation. Na hopping was modeled from an octahedral site into its neighboring octahedral site across a crystallographic face or edge. The initial migration path was constructed with 5 linearly interpolated images. Structural relaxations were performed for the initial and final states. The diffusion barrier

https://dx.doi.org/10.1021/acs.jpcc.0c02274
J. Phys. Chem. C 2020, 124, 12239−12248

was calculated as $\Delta E = E_{max} - E_{initial}$, where E_{max} is the highest energy along the minimum energy pathway and $E_{initial}$ is the energy at the initial state.

The Na diffusivity in pure and doped $NaCrO_2$ was calculated with AIMD simulations and the PBE functional with the $3 \times 3 \times 1$ supercells and at a 2/3 Na concentration. U parameters were not used in the AIMD simulations. To balance accuracy and efficiency, the planewave energy cutoff was set at 400 eV. A Gamma only **k**-point mesh was used with symmetry turned off. Non-spin-polarized calculation was performed for the AIMD calculations as the spin effect is weak at elevated temperatures. AIMD simulations were performed with a time step of 2 fs and at five different temperatures (1500, 1200, 1000, 900, and 720 K). The initial structure was equilibrated from 0 to 1500 K with a period of 1 ps. Then, a Nosé−Hoover thermostat was employed to perform AIMD simulations until the diffusion coefficient is converged. After equilibrating the $NaCrO_2$ systems for at least 40 ps, the Na diffusivity was calculated as the mean squared displacement (MSD) of Na atoms over the time interval t:

$$D = \frac{1}{2dt}\langle [r(t)]^2 \rangle$$

where d is the dimension (3) of the lattice that diffusion takes place. $\langle [r(t)]^2 \rangle$ is the average MSD:

$$\langle [r(t)]^2 \rangle = \frac{1}{N} \sum_i \langle [r_i(t + t_0)]^2 - [r_i(t_0)]^2 \rangle$$

where $r_i(t)$ is the displacement of the ith Na atom at time t, N is the number of diffusion Na atoms, and the bracket means averaging over t. The value of diffusion coefficient D is found from a linear fit of the MSD at different temperatures with respect to $2dt$.

3. RESULTS

3.1. Structures of Pure and Doped $NaCrO_2$. Structural parameters of intercalated layered structures play a critical role in their diffusion kinetics. Table 1 compares the lattice parameters of pure $NaCrO_2$ from various functionals with experiment.[46] Consistent with the general trend of GGA results, both PBE and PBE+U overestimate the lattice parameters. The vdW-inclusive functionals tend to give slightly smaller c than experiment. Among them, the D3/BJ results show the best agreement with experiment.[9,46] The Becke and Johnson damping in D3/BJ corrects the unphysical repulsion between atoms at medium distances in D3 and thus improves predictions of lattice parameters.[35] D3/BJ also predicts an accurate c/a ratio while all other functionals underestimate the ratio. In the "opt" functionals, the steepness of the exchange enhancement factor (F_x) at small reduced density gradient is correlated with stronger repulsion at short interatomic separations. optPBE has steeper F_x than both optB86b and optB88 and predicts larger a, c, and d_{O-O} for $NaCrO_2$. The hybrid density functional HSE06 slightly underestimate c, but overestimate the important d_{O-O}.

Table 1. Lattice Parameters and Interlayer Distance d_{O-O} of Pure $NaCrO_2$ from Calculations and Experiment

	a (Å)	c (Å)	c/a ratio	d_{O-O} (Å)
PBE	3.0237	15.9692	5.281	3.245
PBE+U	3.0451	16.0929	5.285	3.245
D2	3.0026	15.7918	5.259	3.155
D3	3.0474	16.1004	5.283	3.186
D3/BJ	2.9950	15.9497	5.325	3.177
SCAN	2.9950	15.7473	5.258	3.167
optB86b	3.0205	15.9123	5.268	3.191
optB88	3.0088	15.9290	5.294	3.178
optPBE	3.0444	16.0487	5.271	3.219
HSE06	2.9887	15.8938	5.318	3.229
experiment[46]	2.976	15.964	5.364	3.15

Partially desodiated $NaCrO_2$, where eight of the nine Na atoms in the top Na layer were removed from the $3 \times 3 \times 1$ $NaCrO_2$ supercell, was then optimized with these functionals. The vdW effects become more significant in the desodiated structure. Figure 2 and Table S1 compare the structural parameters of the desodiated $NaCrO_2$ from different functionals. Compared to PBE+U, all vdW-inclusive functionals predict moderately reduced lattice parameters (2−3%). The standard deviation of lattice parameters from vdW-inclusive functionals is 0.021 and 0.061 Å for a and c, respectively. However, the change in the interlayer distances for the desodiated $NaCrO_2$ is much more dramatic. The reduction in d_{Cr-Cr} or d_{O-O} ranges from 4% to 15% with different vdW-inclusive functionals. It is well-known that vdW interactions have to be considered to predict correct interlayer distances in layered 2D materials.[47] In deintercalated layered oxides, the decreased ionic bonding elevates the role of vdW interactions, which also has to be accounted for in structural optimizations. A similar reduction in the interlayer distances has been found with vdW-inclusive functionals in delithiated $LiCoO_2$.[26] SCAN, which partially corrects vdW interactions based on semilocal electron kinetic energy gradient, has shown improvement in structural predictions of layered $LiNiO_2$, $LiCoO_2$, and $LiMnO_2$ than PBE+U.[48] For partially desodiated $NaCrO_2$, the

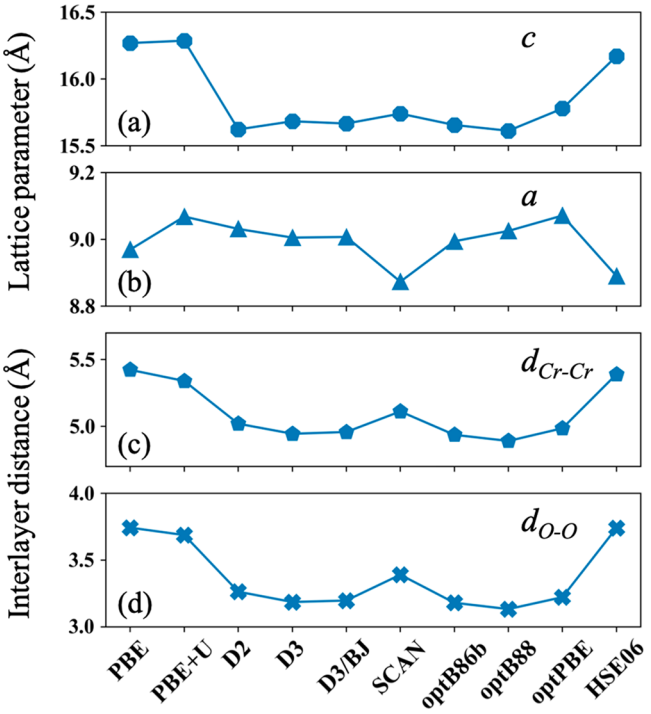

Figure 2. Lattice parameters and interlayer distances of partially desodiated pure $NaCrO_2$ from PBE, PBE+U, vdW-inclusive, and HSE06 functionals.

https://dx.doi.org/10.1021/acs.jpcc.0c02274
J. Phys. Chem. C 2020, 124, 12239−12248

lattice parameters and interlayer distances from SCAN lie between the PBE+U and other vdW-inclusive functionals. HSE06 without vdW corrections predict similar interlayer distances as PBE and PBE+U.

To understand the effects of dopant on the $NaCrO_2$ structure, the lattice parameters for Al-, Co-, Zn-, Mn-, and Ni-doped $NaCrO_2$ were calculated with PBE+U and listed in Table 2. The single-dopant configuration which replaces one Cr atom below the Na layer with one dopant atom was used to model a dilute doping condition. Doping atoms with smaller ionic radii (e.g., Al^{3+} and Co^{3+}) tend to reduce the lattice parameters of $NaCrO_2$, whereas larger doping ions (e.g., Mn^{3+}) increase them. By comparing Table 1 and 2 we find that (i) the Al dopant reduces *a* but increases *c*; (ii) the Ni dopant reduces both *a* and *c*; and (iii) the Mn and Zn dopant increases both *a* and *c*. While the lattice parameters of doped $NaCrO_2$ are correlated with the ionic radius of the dopant, the overall change in lattice parameters is quite small. We note there is no clear correlation between the dopant-oxygen bond length and lattice parameter. For example, the average Al−O bond length (1.98 Å) is much smaller than Zn−O (2.14 Å) in doped $NaCrO_2$, but the lattice parameter difference between Al and Zn-$NaCrO_2$ is less than 0.01 Å. In this study, dopant atoms are not treated as charged defects because our density of states (DOS) calculations (Figure S1) and previous studies[49,50] indicate an easy insulator−metal transformation upon the Na or Li extraction from layered TM oxides.

Table 2. Lattice Parameters of Doped $NaCrO_2$ with PBE+U

	a (Å)	*c* (Å)	*c*/*a* ratio
Al-$NaCrO_2$	3.0398	16.0943	5.295
Co-$NaCrO_2$	3.0399	16.0853	5.291
Ni-$NaCrO_2$	3.0435	16.0823	5.284
Mn-$NaCrO_2$	3.0469	16.0962	5.283
Zn-$NaCrO_2$	3.0447	16.0932	5.286

3.2. Thermodynamic Stability of Doped $NaCrO_2$. The thermodynamic stability of doped $NaCrO_2$ is estimated from the decomposition energy in Table 3. All single-dopant $NaCrO_2$ configurations have low decomposition energy (with GGA+U) below 0.01 eV/atom, suggesting $NaCrO_2$ with a low dopant concentration is experimentally accessible and stable at finite temperatures. The stability of doped $NaCrO_2$ could change with the increase of dopant concentration. Among the studied $NaCrO_2$, Zn-$NaCrO_2$ is the least stable despite a small change in its lattice parameters. The decomposition products of Al- and Mn-$NaCrO_2$ are stable $NaMO_2$ (M = Al and Mn) and $NaCrO_2$, but Ni- and Zn-$NaCrO_2$ decompose to other sodium chromium oxides.

Table 3. Decomposition Energy and Decomposition Products for Single-Dopant $NaCrO_2$

	E_{decomp} (eV/atom)	decomposition products
Al-$NaCrO_2$	0.003	$NaAlO_2$, $NaCrO_2$
Co-$NaCrO_2$	0	none
Ni-$NaCrO_2$	0.003	Na_2CrO_4, Na_4CrO_4, $NaCrO_2$, NiO
Mn-$NaCrO_2$	0.005	$NaMnO_2$, $NaCrO_2$
Zn-$NaCrO_2$	0.008	Na_2CrO_4, Na_4CrO_4, $NaCrO_2$, ZnO

3.3. Diffusion Barrier and Pathway in Doped $NaCrO_2$. Figure 3 compares the Na diffusion barriers in pure and doped $NaCrO_2$ from CI-NEB calculations using the PBE and vdW-inclusive functionals. We selected the vdW functionals for NEB calculations based on calculated structural parameters from section 3.1. D3/BJ gives the closest prediction of lattice parameters and interlayer distances for pure $NaCrO_2$ to experimental values. Two other vdW-inclusive functionals were chosen as comparisons: D3 predicts smaller interlayer distances d_{Cr-Cr} and d_{O-O} while optPBE predicts larger d_{Cr-Cr} and d_{O-O}. The full results of diffusion barriers and interlayer distances are included in Table S2.

The PBE results in Figure 3a show that pure $NaCrO_2$ possesses the highest Na diffusion barrier at 0.44 eV. The reduction in the Na diffusion barrier is significant when a dopant metal cation is near the diffusion pathway, ranging from 27% (Al-$NaCrO_2$) to almost 60% (Co-$NaCrO_2$). Compared to the PBE barrier, the calculated diffusion barriers of pure and doped $NaCrO_2$ are much higher from the vdW-inclusive functionals. The diffusion barrier for pure $NaCrO_2$ rises by 76% to 0.77 eV with D3. This 0.3 eV difference in diffusion barrier could increase the Na diffusivity by several orders of magnitude at room temperature as predicted by the Arrhenius equation. Similarly, the optPBE and D3/BJ functionals increase the diffusion barrier of pure $NaCrO_2$ to 0.71 and 0.76 eV, respectively. However, in all cases, the vdW-inclusive functionals still predict lower Na diffusion barriers in doped $NaCrO_2$ than pure $NaCrO_2$. For example, the diffusion barrier of Al-$NaCrO_2$ is consistently about 0.1 eV lower than pure $NaCrO_2$ from both PBE and vdW-inclusive functionals. The ranking of predicted diffusion barriers among doped $NaCrO_2$ is slightly different among the vdW-inclusive functionals. For example, the Na diffusion barrier in Zn-$NaCrO_2$ is 0.103 eV higher than Co-$NaCrO_2$ from PBE but is 0.017 eV lower from D3.

To elucidate the role of vdW interactions and interlayer distances on the Na diffusion barrier, CI-NEB calculations were performed using PBE but with the lattice parameters optimized from vdW-inclusive functionals (Figure 3c,f). In these calculations, we first optimized the initial and final states with D3/BJ or optPBE and then switched to PBE for transition state calculations. The predicted diffusion barriers from PBE@D3/BJ and PBE@optPBE follow the same trend as D3/BJ and optPBE. PBE@D3/BJ merely increases the diffusion barrier over D3/BJ by 0.05 to 0.07 eV while PBE@optPBE just reduces the diffusion barrier over optPBE by 0.05 to 0.09 eV. Take pure $NaCrO_2$ as an example, PBE@D3/BJ and PBE@optPBE increase or reduce the barriers by only about 8%, respectively. Such small differences are within the numerical uncertainty of most NEB calculations.

Two Na diffusion pathways (Figures 1 and 3) were predicted from CI-NEB calculations in pure and doped $NaCrO_2$. In the oxygen dumbbell hop (ODH), Na migrates to the adjacent octahedral site through a pair of dumbbell oxygen ions (shared edge). In the tetrahedral site hop (TSH), Na migrates to the neighboring octahedral site through a tetrahedron that these sites shared.[51] PBE results indicate the diffusion pathway for pure and Al-$NaCrO_2$ almost follows a straight line (ODH) while the doped $NaCrO_2$ display a sharp elbow at the center of the diffusion pathway (TSH). The local minimum in the diffusion barrier curve for Co-$NaCrO_2$ corresponds to the sharp turn at the tetrahedron site above the doping atom in the Na diffusion pathway. Similar TSH diffusion pathways for Mn- and Zn-$NaCrO_2$ do not produce a local minimum in diffusion barrier curves. The diffusion

https://dx.doi.org/10.1021/acs.jpcc.0c02274
J. Phys. Chem. C 2020, 124, 12239−12248

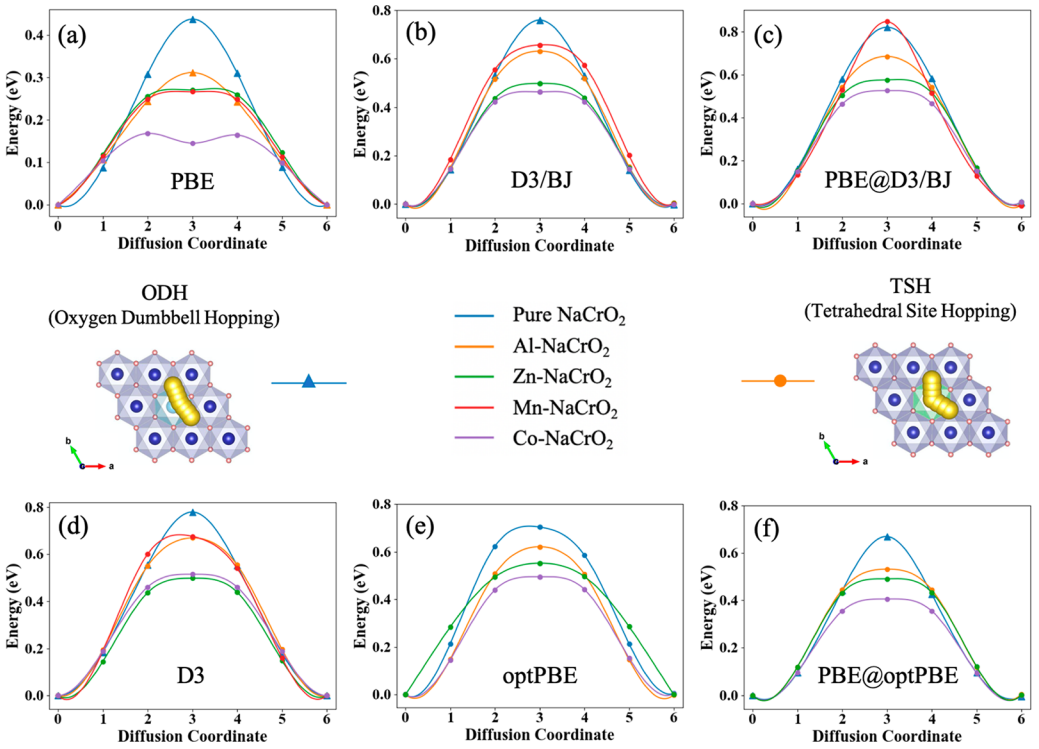

Figure 3. Calculated diffusion barrier for pure and doped $NaCrO_2$ from (a) PBE, (b) D3/BJ, (d) D3, and (e) optPBE functional. Panels c and f are PBE calculated NEB results with the end point structures relaxed by vdW-inclusive functionals D3/BJ and optPBE (abbreviated as PBE@D3/BJ and PBE@optPBE). The triangle and dot symbols represent predicted ODH and TSH diffusion pathway, respectively. Note that vdW-inclusive functionals produce higher diffusion barriers than PBE. The optPBE results of Mn-$NaCrO_2$ are not shown because of convergence issues.

pathway from vdW-inclusive functionals for some doped $NaCrO_2$ are slightly different from the PBE results, but as will be discussed later, the diffusion pathway is not the only factor determining the diffusion barrier.

The CI-NEB calculations reveal the diffusion barrier at a dilute Na concentration, but realistic cycling conditions usually take place with much higher Na concentrations in $NaCrO_2$. Figure 4 shows the Na diffusivity from AIMD simulations for pure, Al- and Co-$NaCrO_2$ for a nondilute Na concentration. In these simulations, a low-energy configuration with 2/3 of the Na sites being occupied on each layer was used as the initial structure.[25] The concentration and position of the dopant atom is the same as in the CI-NEB calculations. The energy convergence was checked at the end of the AIMD simulations. At higher temperatures, e.g., 1000 K, Co-$NaCrO_2$ outperforms pure $NaCrO_2$ in terms of Na diffusivity while Al-$NaCrO_2$ underperforms. The Na ionic conductivity at room temperature was determined from a linear fitting of the logarithm of diffusivities vs temperature and extrapolation to room temperature. At 300 K, the Na diffusivities in Co- and Al-$NaCrO_2$ are 6.92×10^{-9} and 4.33×10^{-9} cm^2/s, both higher than that for pure $NaCrO_2$ at 9.25×10^{-10} cm^2/s by almost 1 order of magnitude. The Na ionic conductivity in Co-$NaCrO_2$ calculated by the Nernst−Einstein equation is 0.67 mS cm^{-1}, an encouraging conductivity value among layered TM oxides. The activation energies of Na diffusion in pure, Co-, and Al-$NaCrO_2$ are obtained from the slope of the fitted line, which are 0.35, 0.29, and 0.28 eV, respectively. The activation energies derived from AIMD follow the same trend as the diffusion barriers from CI-NEB calculations.

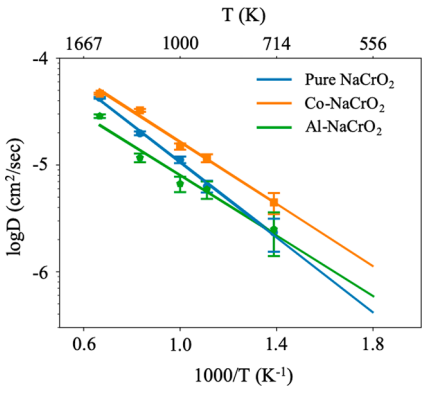

Figure 4. Arrhenius plot of Na diffusivity in pure, Al-, and Co-$NaCrO_2$. The blue, orange, and green lines represent pure, Co- and Al-$NaCrO_2$ with an activation energy of 0.35, 0.29, and 0.28 eV for Na diffusion, respectively.

4. DISCUSSIONS

4.1. Structural Factors for Diffusion Barrier in Doped $NaCrO_2$. The interlayer distance is a major structural factor that determines the diffusion barrier of intercalated atoms in layered TM oxides. It was found that a 200% increase in the Li diffusion barrier is caused by just 4% shrinkage of the Li interlayer distance in $LiCoO_2$.[24] Figure 5a summarizes the change of the Na diffusion barrier with interlayer distances (d_{Cr-Cr} and d_{O-O}) at the initial (IS) and transition state (TS) in pure $NaCrO_2$ calculated with PBE and vdW-inclusive functionals. An almost perfect linear relationship is found between the interlayer distances and the Na diffusion barriers from different functionals, with a coefficient of determination (R^2) higher than 0.95 (Table 4). PBE predicts the largest

https://dx.doi.org/10.1021/acs.jpcc.0c02274
J. Phys. Chem. C 2020, 124, 12239−12248

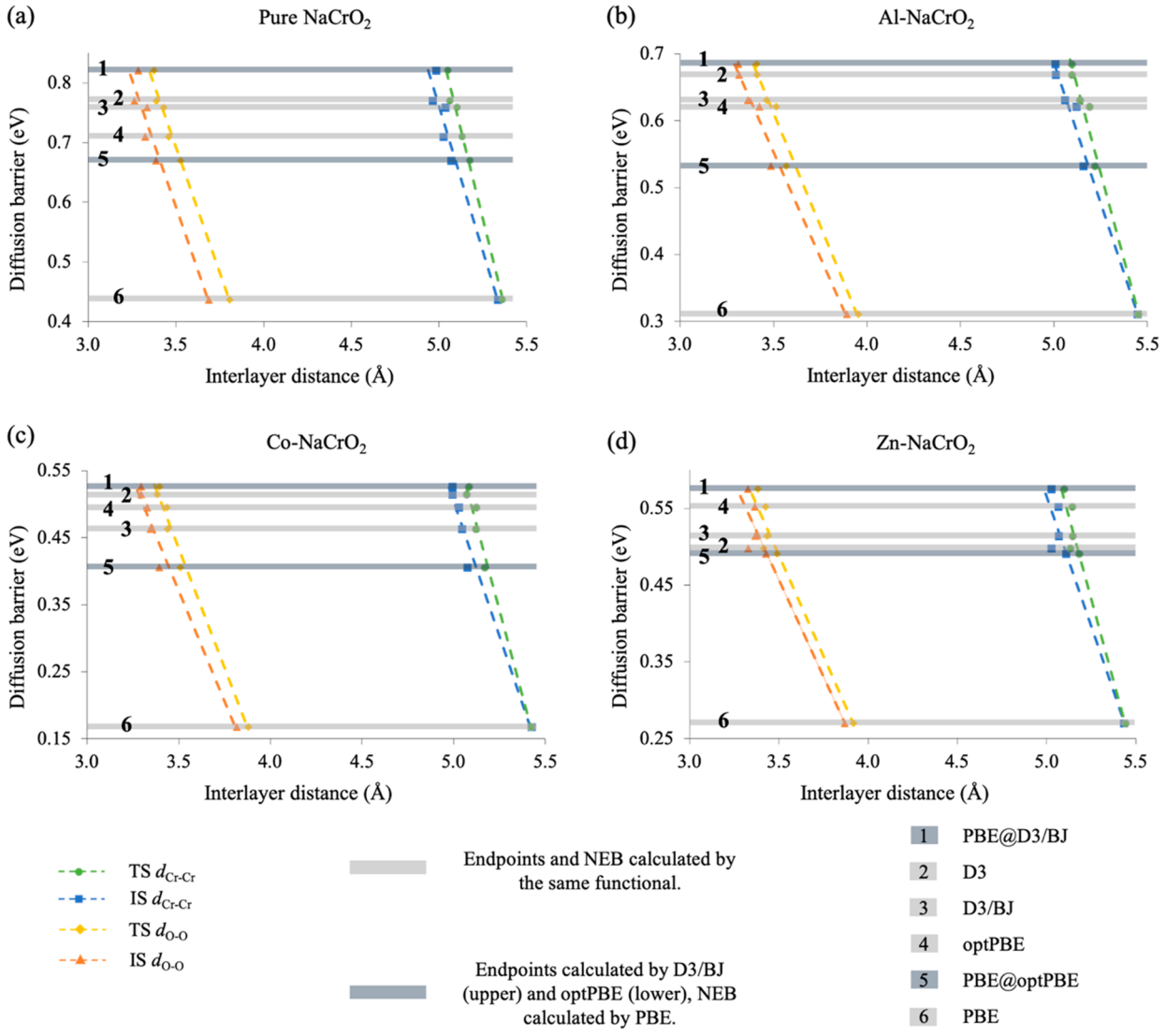

Figure 5. Change of Na diffusion barriers vs interlayer distances d_{Cr-Cr} and d_{O-O} from PBE and vdW inclusive functionals for (a) pure $NaCrO_2$, (b) Al-$NaCrO_2$, (c) Zn-$NaCrO_2$, and (d) Co-$NaCrO_2$. IS and TS correspond to the initial state (before diffusion) and transition state (center of the diffusion pathway) in CI-NEB calculations. The fitted dashed lines in panels a−d from right to left correspond to TS d_{Cr-Cr}, IS d_{Cr-Cr}, TS d_{O-O}, and IS d_{O-O}. The light gray bands represent the end points and NEB calculated by the same functional and dark gray bands represent the end points optimized by vdW-inclusive functionals and NEB calculated by PBE (PBE@D3/BJ and PBE@optPBE).

Table 4. Slope and Coefficient of Determination (R^2) of Fitted Lines in Figure 5

		pure $NaCrO_2$		Al-$NaCrO_2$		Zn-$NaCrO_2$		Co-$NaCrO_2$	
		slope	R^2	slope	R^2	slope	R^2	slope	R^2
IS	d_{Cr-Cr} (Å)	−0.985	0.956	−0.838	0.981	−0.677	0.931	−0.805	0.978
	d_{O-O} (Å)	−0.857	0.956	−0.631	0.983	−0.505	0.937	−0.661	0.979
TS	d_{Cr-Cr} (Å)	−1.190	0.987	−1.037	0.978	−0.855	0.964	−1.022	0.986
	d_{O-O} (Å)	−0.845	0.989	−0.675	0.982	−0.527	0.957	−0.712	0.986

interlayer distances of d_{Cr-Cr} and d_{O-O} at IS and TS, as well as the lowest diffusion barrier among all functionals. In comparison, D3 predicts smaller d_{Cr-Cr} and d_{O-O} at IS by 0.3−0.4 Å, and a much higher Na diffusion barrier. The 88% increase (~0.3 eV) in the Na diffusion barrier coincides with a 7% decrease in the Na interlayer distances when considering vdW interactions. All functionals predict that both d_{Cr-Cr} and d_{O-O} at TS are greater than IS, possibly due to a combination of steric and electrostatic effect that expands the M layer during Na migration.[52] Since the migrating Na atom is directly interacting with O, the d_{Cr-Cr} difference between IS and TS is smaller than d_{O-O} which is more susceptible to change. Because the interlayer distances can be severely overestimated without vdW interactions (Table 1), vdW-inclusive functionals can give more accurate predictions of structural parameters and diffusion barriers in layered TM oxides.

In doped $NaCrO_2$, the Na diffusion barriers from PBE and vdW-inclusive functionals (Figure 5b−d) follow a similar linear trend with the interlayer distances. Among the studied systems, Zn-$NaCrO_2$ exhibits the greatest shrinkage in the interlayer

https://dx.doi.org/10.1021/acs.jpcc.0c02274
J. Phys. Chem. C 2020, 124, 12239−12248

distances with the vdW-inclusive functionals whereas its Na diffusion barriers increases more with these functionals. At IS, a moderate shrinkage in d_{Cr-Cr} (7%) and d_{O-O} (14%) results in an 113% increase in the Na diffusion barrier in Zn-$NaCrO_2$. Similar to pure $NaCrO_2$, the absolute values of the slopes of d_{O-O} with different potentials are lower than d_{Cr-Cr}, suggesting d_{O-O} affects the diffusion barrier more directly. All doped systems have high R^2 scores (>0.93) in the linear fitting, but the slopes of the fitted lines are dependent on the dopant. We find that pure $NaCrO_2$ possesses the largest absolute value of slope for both d_{Cr-Cr} and d_{O-O} at IS, indicating the diffusion barrier for pure $NaCrO_2$ can be sensitive with the interlayer distance changes.

The considerable increase in the Na diffusion barrier from the vdW-inclusive functionals (Figure 6) are partially caused

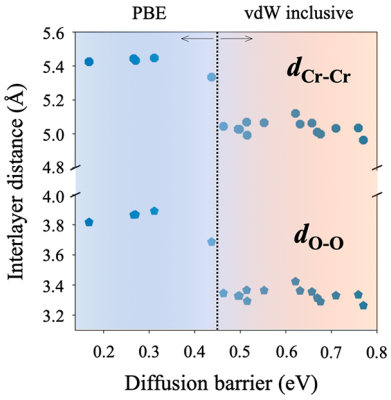

Figure 6. Overall trends of Na diffusion barriers vs interlayer distances d_{Cr-Cr} and d_{O-O} from PBE and vdW-inclusive functionals.

by the reduced interlayer distances from the vdW interactions. Nonetheless, if constrained the interlayer distances from vdW-inclusive calculations, PBE also predicts similarly higher Na diffusion barriers. Our calculations show that the average PBE Na diffusion barrier with D3/BJ interlayer distances is only 0.06 eV higher than the D3/BJ barrier, while the average PBE barrier with optPBE interlayer distances is only 0.07 eV lower than the optPBE barrier. These results indicate that although the vdW interactions play an important role in the interlayer distances in layered TM oxides, the diffusion barrier is still largely determined by short-range non-vdW interactions. We note that the origin of the above linear relationship between Na diffusion barriers vs interlayer distances is different from the change of diffusion barrier due to lattice strain. The vdW calculations optimize the structures with all possible degrees of freedom. As a result, the contraction of the lattice constants from vdW calculations does not produce local strain at the ground state condition. Although the increase in the diffusion barrier is related to the stronger interactions between Na and nearby atoms in the vdW calculations, such results are not a direct effect of local strain.

In addition to the interlayer distances, other structural factors can further influence the Na diffusion barrier in doped $NaCrO_2$. For instance, the Na diffusion barriers between Zn- and Mn-$NaCrO_2$ are very similar from PBE (0.270 vs 0.266 eV), but vdW-inclusive functionals predict a much larger difference in their diffusion barriers (Figure 3): The Na diffusion barrier in Zn-$NaCrO_2$ is 0.143 eV (D3/BJ) or 0.178 eV (D3) lower than Mn-$NaCrO_2$. The difference can be explained by a combination of interlayer distances and other structural factors. First, the interlayer distance d_{O-O} at IS is almost the same for Zn- and Mn-$NaCrO_2$ (3.868 vs 3.866 Å) from PBE, but the reduction of d_{O-O} is stronger for Mn-$NaCrO_2$ with the vdW-inclusive functionals, increasing the d_{O-O} differences to 0.011 Å with D3/BJ and 0.028 Å with D3 and consequently, higher diffusion barriers in Mn-$NaCrO_2$. Second, the change in the geometric features along the diffusion pathway enhances the diffusion barrier differences. Na diffuses via TSH in Zn- and Mn-$NaCrO_2$, so the triangular cross section between the initial Na octahedral site and the intermediate tetrahedral site is critical for Na diffusion. The incircle radius (IR) of the cross-sectional triangle (Figure 1) at IS describes the geometric dimension that allows Na to pass through. PBE predicts the IR to be 1.005 Å for Mn-$NaCrO_2$ and 1.070 Å for Zn-$NaCrO_2$. The IR of Mn-$NaCrO_2$ reduces to 0.96 Å with D3 and D3/BJ, but the IR of Zn-$NaCrO_2$ increases to 1.080 Å (D3) and 1.015 Å (D3/BJ). The change in IR is also correlated with the change of area A_{tet} (Table S3). Considering the interlayer distances are reduced with the vdW-inclusive functionals, the increase in the IR of Zn-$NaCrO_2$ and its effect on the Na diffusion barrier is quite significant.

4.2. Electrostatic Interactions and Diffusion Barrier in Doped $NaCrO_2$. Besides the structural features, the ionic diffusion in layered TM oxides is also influenced by the valence state of TM that exerts electrostatic repulsion along the diffusion pathway.[22] We compare the valence state of Co and Mn in their doped $NaCrO_2$ to understand how electrostatic interactions affect the Na diffusion barrier. In Co- $NaCrO_2$, the Bader charge of the Co site is almost unvaried between the fully intercalated state (7.770 e) and the partially desodiated state (7.728 e). DOS (Figure S1f) suggests the Co dopant in the desodiated state adopts the low-spin configuration and maintain its valence state of 3+. Meanwhile, the total Bader charge of the screening oxygen layer between the TM and Na layer in Co-$NaCrO_2$ (63.087 e) is the lowest among all pure and doped $NaCrO_2$ (Table S4). The combination of reduced electrostatic repulsion due to a low valence state of Co and weakened O−Na interactions can explain the lowest diffusion barrier in Co-$NaCrO_2$ among the doped $NaCrO_2$. In Mn-$NaCrO_2$, which has a relatively high Na diffusion barrier, the valence state of Mn changes from 3+ to 4+ during the desodiation process. Such a change in valence state is supported by the DOS analysis (Figure S1d), where a high spin d^4 configuration of t_{2g}^3 e_g^1 changes to a d^3 electronic configuration of t_{2g}^3 e_g^0 for the Mn site, as well as a change of the magnetic moment from 4.09 μ_B to 3.32 μ_B and a reduction in the Bader charge of the Mn site (Table S4). The high valent Mn cation can excert stronger electrostatic interaction with the migrating Na and contribute to the high diffusion barrier of Mn-$NaCrO_2$.[24]

4.3. Diffusion Pathways in Doped $NaCrO_2$. Previous studies on layered TM oxides correlates ODH with high intercalate concentration and single-site vacancy, while TSH with low intercalate concentration and divacancy.[51,53,54] ODH usually shows a higher diffusion barrier than TSH in a dilute vacancy condition.[54] In this study, we consider Na diffusion in a dilute intercalation condition where neighboring vacancies are readily available, corresponding to a multivacancy condition. Surprisingly, TSH was still predicted in some systems and were sometimes affected by the choice of functionals that include vdW interactions. For example, the Na diffusion pathway in pure $NaCrO_2$ changes from ODH (PBE, D3, and D3/BJ) to TSH (optPBE) as shown in Figure

https://dx.doi.org/10.1021/acs.jpcc.0c02274
J. Phys. Chem. C 2020, 124, 12239−12248

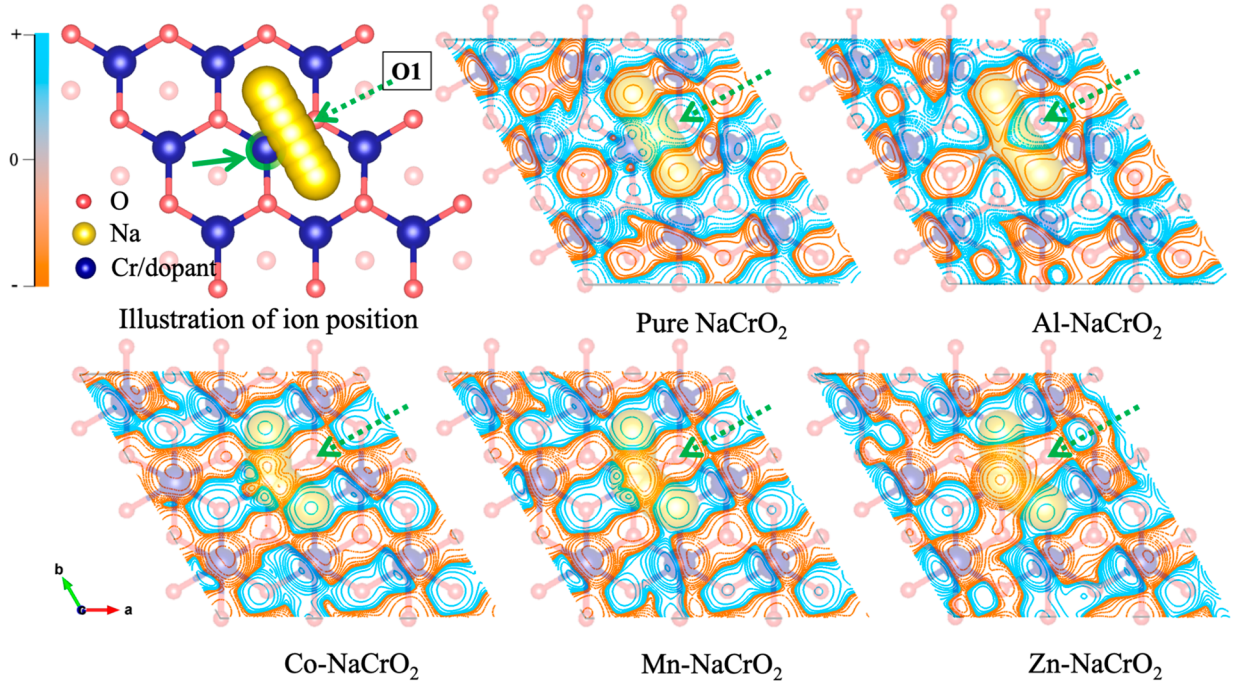

Figure 7. Charge-density difference plot for pure and doped $NaCrO_2$ when Na is at TS between TSH and ODH diffusion pathway. The cross sections are cut along the [001] direction of the Cr layer below the Na layer that the dopant sits. The solid green arrow points the Cr site that is substituted with dopant in doped $NaCrO_2$. The charge density change from ODH to TSH is positive in the blue area and negative in the orange area. The density of the contour circles is proportional to the change of charge density. O1 is in the oxygen layer (solid pink) between the Na and Cr layer and the oxygen layer below the Cr layer is in light pink.

1. In Al-$NaCrO_2$, PBE predicts an ODH diffusion pathway whereas all vdW-inclusive functionals predict a TSH diffusion pathway. We found that functionals (e.g., PBE) predicting larger interlayer distances also tend to predict ODH as the preferred diffusion pathway.

The Na diffusion pathway is also influenced by local charge distributions near the dopants. The charge-density difference plot in Figure 7 is generated by subtracting the ODH charge density from the TSH charge density at the transition state. The charge-density distribution is plotted by projecting along the [001] direction at the Cr layer below the Na layer. The blue circles represent positive charge density changes from ODH to TSH. The charge density near the O atoms directly interacting with the Na atom during diffusion is influenced by the species of the neighboring dopants to Na and affects the diffusion pathway. For example, the charge density in the Cr layer below the O1 atom is decreased in the preferred ODH pathway (blue) for pure and Al-$NaCrO_2$, indicating an increased charge density and stronger interactions between the O1 atom and the migrating Na atom at the transition state in the ODH pathway. Such stronger interactions suggest a lower energy for the transition state in ODH and a lower diffusion barrier. The charge-density difference at the same position is reversed for dopants that prefer the TSH pathway. In comparison, the trend of charge density difference in the Cr layer above the Na layer (no dopant) does not change in different doped systems (Figure S2), confirming the effect on charge density distribution is caused by dopant. The charge-density difference distribution can qualitatively predict the diffusion pathways in doped layered TM oxides which are important for the design of layered cathode materials.

5. CONCLUSIONS

First-principles calculations were performed to study the stability and Na diffusivity of doped O3-$NaCrO_2$ with PBE and vdW-inclusive functionals. The NEB and AIMD results indicate that low-concentration metal doping can reduce the Na diffusion barrier and improve diffusivity in $NaCrO_2$. It is necessary to consider the vdW interactions when predicting the interlayer distances in partially deintercalated layered structures. The vdW-inclusive functionals consistently predict lower interlayer distances than PBE. The interlayer distances have a significant effect on Na diffusion barriers and pathways. A linear relation is found between the interlayer distances and the diffusion barriers with different functionals. Among the studied doped systems, Co-$NaCrO_2$ outperforms the other doped $NaCrO_2$ with a lower Na diffusion barrier and can be a promising candidate for high-rate Na-ion cathode materials.

■ ASSOCIATED CONTENT

Supporting Information

The Supporting Information is available free of charge at https://pubs.acs.org/doi/10.1021/acs.jpcc.0c02274.

Additional results as reported in Tables S1−S4 and Figures S1 and S2 (PDF)

■ AUTHOR INFORMATION

Corresponding Author

Wei Chen − *Department of Mechanical, Materials and Aerospace Engineering, Illinois Institute of Technology, Chicago, Illinois 60616, United States;* orcid.org/0000-0002-1135-7721; Email: wei.chen@iit.edu

https://dx.doi.org/10.1021/acs.jpcc.0c02274
J. Phys. Chem. C 2020, 124, 12239−12248

Authors

Jialiang Wei − *Department of Mechanical, Materials and Aerospace Engineering, Illinois Institute of Technology, Chicago, Illinois 60616, United States*

Leon Shaw − *Department of Mechanical, Materials and Aerospace Engineering, Illinois Institute of Technology, Chicago, Illinois 60616, United States;* orcid.org/0000-0002-2170-1573

Complete contact information is available at: https://pubs.acs.org/10.1021/acs.jpcc.0c02274

Notes

The authors declare no competing financial interest.

■ ACKNOWLEDGMENTS

The authors gratefully acknowledge the support by the National Science Foundation under Grant No. DMR-1709959. This research used resources of the National Energy Research Scientific Computing Center (NERSC), a U.S. Department of Energy Office of Science User Facility operated under Contract No. DE-AC02-05CH11231. This work used the Extreme Science and Engineering Discovery Environment (XSEDE), which is supported by National Science Foundation Grant No. ACI-1548562.

■ REFERENCES

(1) Delmas, C. Sodium and Sodium-Ion Batteries: 50 Years of Research. *Adv. Energy Mater.* **2018**, *8*, 1703137.

(2) Ellis, B. L.; Nazar, L. F. Sodium and Sodium-Ion Energy Storage Batteries. *Curr. Opin. Solid State Mater. Sci.* **2012**, *16* (4), 168−177.

(3) Berthelot, R.; Carlier, D.; Delmas, C. Electrochemical Investigation of the P2−Na x CoO2 Phase Diagram. *Nat. Mater.* **2011**, *10* (1), 74−80.

(4) Yabuuchi, N.; Kajiyama, M.; Iwatate, J.; Nishikawa, H.; Hitomi, S.; Okuyama, R.; Usui, R.; Yamada, Y.; Komaba, S. P2-Type Na x [Fe1/2Mn1/2]O2Made from Earth-Abundant Elements for Rechargeable Na Batteries. *Nat. Mater.* **2012**, *11* (6), 512−517.

(5) Kim, S.-W.; Seo, D.-H.; Ma, X.; Ceder, G.; Kang, K. Electrode Materials for Rechargeable Sodium-Ion Batteries: Potential Alternatives to Current Lithium-Ion Batteries. *Adv. Energy Mater.* **2012**, *2* (7), 710−721.

(6) Lu, Z.; Dahn, J. R. In Situ X-Ray Diffraction Study of P2-Na[Sub 2/3][Ni[Sub 1/3]Mn[Sub 2/3]]O[Sub 2]. *J. Electrochem. Soc.* **2001**, *148* (11), A1225.

(7) Carlier, D.; Cheng, J. H.; Berthelot, R.; Guignard, M.; Yoncheva, M.; Stoyanova, R.; Hwang, B. J.; Delmas, C. The P2-Na2/3Co2/3Mn1/3O2 Phase: Structure, Physical Properties and Electrochemical Behavior as Positive Electrode in Sodium Battery. *Dalt. Trans.* **2011**, *40* (36), 9306.

(8) Kim, D.; Kang, S.; Slater, M.; Rood, S.; Vaughey, J. T.; Karan, N.; Balasubramanian, M.; Johnson, C. S. Enabling Sodium Batteries Using Lithium-Substituted Sodium Layered Transition Metal Oxide Cathodes. *Adv. Energy Mater.* **2011**, *1* (3), 333−336.

(9) Yu, C.-Y.; Park, J.-S.; Jung, H.-G.; Chung, K.-Y.; Aurbach, D.; Sun, Y.-K.; Myung, S.-T. NaCrO $_2$ Cathode for High-Rate Sodium-Ion Batteries. *Energy Environ. Sci.* **2015**, *8* (7), 2019−2026.

(10) Shadike, Z.; Zhao, E.; Zhou, Y.-N.; Yu, X.; Yang, Y.; Hu, E.; Bak, S.; Gu, L.; Yang, X.-Q.; Chen, L.; Warburton, R. E.; Chen, K.; Mark, C.; Greeley, J. P.; Elam, J. W.; Chen, L.; Warburton, R. E.; Chen, K.; Libera, J. A.; Johnson, C.; Yang, Z.; Hersam, M. C.; Greeley, J. P.; Elam, J. W.; Delmas, C.; Fouassier, C.; Hagenmuller, P.; Wang, L.; Maxisch, T.; Ceder, G. Structural Classification and Properties of the Layered Oxides. *Physica B+C* **1980**, *99* (1−4), 81−85.

(11) Kim, S.; Ma, X.; Ong, S. P.; Ceder, G. A Comparison of Destabilization Mechanisms of the Layered NaxMO2and LixMO2-compounds upon Alkali De-Intercalation. *Phys. Chem. Chem. Phys.* **2012**, *14* (44), 15571−15578.

(12) Komaba, S.; Takei, C.; Nakayama, T.; Ogata, A.; Yabuuchi, N. Electrochemical Intercalation Activity of Layered NaCrO2 vs. LiCrO2. *Electrochem. Commun.* **2010**, *12* (3), 355−358.

(13) Mizushima, K.; Jones, P. C.; Wiseman, P. J.; Goodenough, J. B. LixCoO2 (0 < x<-1): A New Cathode Material for Batteries of High Energy Density. *Mater. Res. Bull.* **1980**, *15* (6), 783−789.

(14) Ceder, G.; Chiang, Y.-M.; Sadoway, D. R.; Aydinol, M. K.; Jang, Y.-I.; Huang, B. Identification of Cathode Materials for Lithium Batteries Guided by First-Principles Calculations. *Nature* **1998**, *392* (6677), 694−696.

(15) Jang, Y.-I.; Huang, B.; Wang, H.; Sadoway, D. R.; Ceder, G.; Chiang, Y.; Liu, H.; Tamura, H. LiAlyCo1−yO2 (R3m) Intercalation Cathode for Rechargeable Lithium Batteries. *J. Electrochem. Soc.* **1999**, *146* (3), 862.

(16) Tukamoto, H.; West, A. R. Electronic Conductivity of LiCoO2 and Its Enhancement by Magnesium Doping. *J. Electrochem. Soc.* **1997**, *144* (9), 3164.

(17) Hu, S.-K.; Chou, T.-C.; Hwang, B.-J.; Ceder, G. Effect of Co Content on Performance of LiAl1/3−xCoxNi1/3Mn1/3O2 Compounds for Lithium-Ion Batteries. *J. Power Sources* **2006**, *160* (2), 1287−1293.

(18) Guilmard, M.; Croguennec, L.; Denux, D.; Delmas, C. Thermal Stability of Lithium Nickel Oxide Derivatives. Part I: Li XNi1.02O2 and LixNi 0.89Al0.16O2 (x = 0.50 and 0.30). *Chem. Mater.* **2003**, *15* (23), 4476−4483.

(19) Wu, X.; Xu, G.-L.; Zhong, G.; Gong, Z.; McDonald, M. J.; Zheng, S.; Fu, R.; Chen, Z.; Amine, K.; Yang, Y. Insights into the Effects of Zinc Doping on Structural Phase Transition of P2-Type Sodium Nickel Manganese Oxide Cathodes for High-Energy Sodium Ion Batteries. *ACS Appl. Mater. Interfaces* **2016**, *8* (34), 22227−22237.

(20) Yan, W.; Xie, Y.; Jiang, J.; Sun, D.; Ma, X.; Lan, Z.; Jin, Y. Enhanced Rate Performance of Al-Doped Li-Rich Layered Cathode Material via Nucleation and Post-Solvothermal Method. *ACS Sustainable Chem. Eng.* **2018**, *6* (4), 4625−4632.

(21) Liu, H.; Cao, Q.; Fu, L. J.; Li, C.; Wu, Y. P.; Wu, H. Q. Doping Effects of Zinc on LiFePO4 Cathode Material for Lithium Ion Batteries. *Electrochem. Commun.* **2006**, *8* (10), 1553−1557.

(22) Kang, K. Electrodes with High Power and High Capacity for Rechargeable Lithium Batteries. *Science* **2006**, *311* (5763), 977−980.

(23) Ong, S. P.; Chevrier, V. L.; Hautier, G.; Jain, A.; Moore, C.; Kim, S.; Ma, X.; Ceder, G. Voltage, Stability and Diffusion Barrier Differences between Sodium-Ion and Lithium-Ion Intercalation Materials. *Energy Environ. Sci.* **2011**, *4* (9), 3680.

(24) Kang, K.; Ceder, G. Factors That Affect Li Mobility in Layered Lithium Transition Metal Oxides. *Phys. Rev. B: Condens. Matter Mater. Phys.* **2006**, *74* (9), 1−7.

(25) Mo, Y.; Ong, S. P.; Ceder, G. Insights into Diffusion Mechanisms in P2 Layered Oxide Materials by First-Principles Calculations. *Chem. Mater.* **2014**, *26* (18), 5208−5214.

(26) Aykol, M.; Kim, S.; Wolverton, C. van der Waals Interactions in Layered Lithium Cobalt Oxides. *J. Phys. Chem. C* **2015**, *119* (33), 19053−19058.

(27) Carrasco, J. Role of van Der Waals Forces in Thermodynamics and Kinetics of Layered Transition Metal Oxide Electrodes: Alkali and Alkaline-Earth Ion Insertion into V 2 O 5. *J. Phys. Chem. C* **2014**, *118* (34), 19599−19607.

(28) Blöchl, P. E. Projector Augmented-Wave Method. *Phys. Rev. B: Condens. Matter Mater. Phys.* **1994**, *50* (24), 17953−17979.

(29) Kresse, G.; Furthmüller, J. Efficiency of Ab-Initio Total Energy Calculations for Metals and Semiconductors Using a Plane-Wave Basis Set. *Comput. Mater. Sci.* **1996**, *6* (1), 15−50.

(30) Kresse, G.; Furthmüller, J. Efficient Iterative Schemes for Ab Initio Total-Energy Calculations Using a Plane-Wave Basis Set. *Phys. Rev. B: Condens. Matter Mater. Phys.* **1996**, *54* (16), 11169−11186.

(31) Perdew, J. P.; Burke, K.; Ernzerhof, M. Generalized Gradient Approximation Made Simple. *Phys. Rev. Lett.* **1996**, *77* (18), 3865−3868.

(32) Perdew, J. P.; Ernzerhof, M.; Burke, K. Rationale for Mixing Exact Exchange with Density Functional Approximations. *J. Chem. Phys.* **1996**, *105* (22), 9982.
(33) Grimme, S. Semiempirical GGA-Type Density Functional Constructed with a Long-Range Dispersion Correction. *J. Comput. Chem.* **2006**, *27* (15), 1787−1799.
(34) Grimme, S.; Antony, J.; Ehrlich, S.; Krieg, H. A Consistent and Accurate Ab Initio Parametrization of Density Functional Dispersion Correction (DFT-D) for the 94 Elements H-Pu. *J. Chem. Phys.* **2010**, *132* (15), 154104.
(35) Grimme, S.; Ehrlich, S.; Goerigk, L. Effect of the Damping Function in Dispersion Corrected Density Functional Theory. *J. Comput. Chem.* **2011**, *32* (7), 1456−1465.
(36) Sun, J.; Ruzsinszky, A.; Perdew, J. P. Strongly Constrained and Appropriately Normed Semilocal Density Functional. *Phys. Rev. Lett.* **2015**, *115* (3), 036402.
(37) Klimeš, J.; Bowler, D. R.; Michaelides, A. Van Der Waals Density Functionals Applied to Solids. *Phys. Rev. B: Condens. Matter Mater. Phys.* **2011**, *83* (19), 195131.
(38) Anisimov, V. I.; Aryasetiawan, F.; Lichtenstein, A. I. First-Principles Calculations of the Electronic Structure and Spectra of Strongly Correlated Systems: The **LDA** + *U* Method. *J. Phys.: Condens. Matter* **1997**, *9* (4), 767−808.
(39) Wang, L.; Maxisch, T.; Ceder, G. Oxidation Energies of Transition Metal Oxides within the GGA+U Framework. *Phys. Rev. B: Condens. Matter Mater. Phys.* **2006**, *73* (19), 1−6.
(40) Jain, A.; Ong, S. P.; Hautier, G.; Chen, W.; Richards, W. D.; Dacek, S.; Cholia, S.; Gunter, D.; Skinner, D.; Ceder, G.; Persson, K. A. Commentary: The Materials Project: A Materials Genome Approach to Accelerating Materials Innovation. *APL Mater.* **2013**, *1* (1), 011002.
(41) Dudarev, S. L.; Botton, G. A.; Savrasov, S. Y.; Humphreys, C. J.; Sutton, A. P. Electron-Energy-Loss Spectra and the Structural Stability of Nickel Oxide: An LSDA+U Study. *Phys. Rev. B: Condens. Matter Mater. Phys.* **1998**, *57* (3), 1505−1509.
(42) Heyd, J.; Scuseria, G. E.; Ernzerhof, M. Hybrid Functionals Based on a Screened Coulomb Potential. *J. Chem. Phys.* **2003**, *118* (18), 8207−8215.
(43) Heyd, J.; Scuseria, G. E.; Ernzerhof, M. Erratum: Hybrid Functionals Based on a Screened Coulomb Potential. *J. Chem. Phys.* **2003**, *118*, 8207.
(44) Ong, S. P.; Richards, W. D.; Jain, A.; Hautier, G.; Kocher, M.; Cholia, S.; Gunter, D.; Chevrier, V. L.; Persson, K. A.; Ceder, G. Python Materials Genomics (Pymatgen): A Robust, Open-Source Python Library for Materials Analysis. *Comput. Mater. Sci.* **2013**, *68*, 314−319.
(45) Henkelman, G.; Uberuaga, B. P.; Jónsson, H. A Climbing Image Nudged Elastic Band Method for Finding Saddle Points and Minimum Energy Paths. *J. Chem. Phys.* **2000**, *113* (22), 9901.
(46) Komaba, S.; Nakayama, T.; Ogata, A.; Shimizu, T.; Takei, C.; Takada, S.; Hokura, A.; Nakai, I. Electrochemically Reversible Sodium Intercalation of Layered NaNi 0.5Mn0.5O2 and NaCrO2. *ECS Trans* **2008**, *16* (42), 43−55.
(47) Bučko, T.; Lebègue, S.; Hafner, J.; Ángyán, J. G. Tkatchenko-Scheffler van Der Waals Correction Method with and without Self-Consistent Screening Applied to Solids. *Phys. Rev. B: Condens. Matter Mater. Phys.* **2013**, *87* (6), 064110.
(48) Chakraborty, A.; Dixit, M.; Aurbach, D.; Major, D. T. Predicting Accurate Cathode Properties of Layered Oxide Materials Using the SCAN Meta-GGA Density Functional. *npj Comput. Mater.* **2018**, *4* (1), 60.
(49) Molenda, J.; Wilk, P.; Marzec, J. Structural, Electrical and Electrochemical Properties of LiNiO2. *Solid State Ionics* **2002**, *146* (1−2), 73−79.
(50) Marianetti, C. A.; Kotliar, G.; Ceder, G. A First-Order Mott Transition in LixCoO2. *Nat. Mater.* **2004**, *3* (9), 627−631.
(51) Van der Ven, A.; Ceder, G. Lithium Diffusion in Layered LixCoO2. *Electrochem. Solid-State Lett.* **1999**, *3* (7), 301.
(52) Dixit, M.; Kosa, M.; Lavi, O. S.; Markovsky, B.; Aurbach, D.; Major, D. T. Thermodynamic and Kinetic Studies of LiNi0.5 Co0.2Mn0.3O2 as a Positive Electrode Material for Li-Ion Batteries Using First Principles. *Phys. Chem. Chem. Phys.* **2016**, *18* (9), 6799−6812.
(53) Wei, Y.; Zheng, J.; Cui, S.; Song, X.; Su, Y.; Deng, W.; Wu, Z.; Wang, X.; Wang, W.; Rao, M.; Lin, Y.; Wang, C.; Amine, K.; Pan, F. Kinetics Tuning of Li-Ion Diffusion in Layered Li(NixMnyCoz)O2. *J. Am. Chem. Soc.* **2015**, *137* (26), 8364−8367.
(54) Van der Ven, A.; Ceder, G. Lithium Diffusion in Layered LixCoO2. *Electrochem. Solid-State Lett.* **1999**, *3* (7), 301.

https://dx.doi.org/10.1021/acs.jpcc.0c02274
J. Phys. Chem. C 2020, 124, 12239−12248